Detection of correlated galaxy ellipticities from CFHT data: first evidence for gravitational lensing by large-scale structures[*]

L. Van Waerbeke[1], **Y. Mellier**[2,3], **T. Erben**[4], **J.C. Cuillandre**[5], **F. Bernardeau**[6], **R. Maoli**[2,3], **E. Bertin**[2,3], **H.J. Mc Cracken**[7], **O. Le Fèvre**[7], **B. Fort**[2], **M. Dantel-Fort**[3], **B. Jain**[8], and **P. Schneider**[4]

[1] Canadian Institut for Theoretical Astrophysics, 60 St Georges Str., Toronto, M5S 3H8 Ontario, Canada
[2] Institut d'Astrophysique de Paris, 98 bis, boulevard Arago, 75014 Paris, France
[3] Observatoire de Paris, DEMIRM, 61, avenue de l'Observatoire, 75014 Paris, France
[4] Max-Planck-Institut für Astrophysik, Karl-Schwarzschild-Strasse 1, Postfach 1523, 85740 Garching, Germany
[5] Canada-France-Hawaii-Telescope, P.O. Box 1597, Kamuela, Hawaii 96743, USA
[6] Service de Physique Théorique, C.E. de Saclay, 91191 Gif sur Yvette Cedex, France
[7] Laboratoire d'Astronomie Spatiale, 13376 Marseille Cedex 12, France
[8] Department of Physics, Johns Hopkins University, Baltimore, MD 21218, USA

Abstract. We report the detection of a significant (5.5 σ) excess of correlations between galaxy ellipticities at scales ranging from 0.5 to 3.5 arc-minutes. This detection of a gravitational lensing signal by large-scale structure was made using a composite high quality imaging survey of 6300 arcmin^2 obtained at the Canada France Hawaii Telescope (CFHT) with the UH8K and CFH12K panoramic CCD cameras. The amplitude of the excess correlation is $2.2 \pm 0.2\%$ at 1 arcmin scale, in agreement with theoretical predictions of the lensing effect induced by large-scale structure. We provide a quantitative analysis of systematics which could contribute to the signal and show that the net effect is small and can be corrected for. In particular, we show that the spurious excess of correlations caused by the residual of the anisotropic Point Spread Function (PSF) correction is well below the measured signal. We show that the measured ellipticity correlations behave as expected for a gravitational shear signal. The relatively small size of our survey precludes tight constraints on cosmological models. However the data are in favor of cluster normalized cosmological models, and marginally reject Cold Dark Matter models with ($\Omega = 0.3$, $\sigma_8 < 0.6$) or ($\Omega = 1$, $\sigma_8 = 1$). The detection of cosmic shear demonstrates the technical feasibility of using weak lensing surveys to measure dark matter clustering and the potential for cosmological parameter measurements, in particular with upcoming wide field CCD cameras.

Key words: cosmology: theory – cosmology: dark matter – cosmology: gravitational lensing – cosmology: large-scale structure of Universe

1. Introduction

The measurement of weak gravitational lensing produced by the large-scale structures in the universe (hereafter, the cosmic shear) is potentially the most effective, albeit challenging, step toward a direct mapping of the dark matter distribution in the universe at intermediate and low redshift. Unlike several popular probes of large-scale structures, lensing maps the dark matter directly, regardless of the distribution of light emitted by gas and galaxies or the dynamical stage of the structures analysed.

A decade of theoretical and technical studies has shown that the gravitational distortion produced by the structures along the lines-of-sight contains important clues on structure formation models (see Mellier 1999, Bartelmann & Schneider 1999a for reviews and references therein). From these studies, we know that weak lensing can provide measurements of cosmological parameters and the shape of the projected density power spectrum (Blandford et al. 1991, Miralda-Escude 1991, Kaiser 1992, Villumsen 1996, Bernardeau et al. 1997, Jain & Seljak 1997, Kaiser 1998, Schneider et al. 1998, Jain et al. 1999, Van Waerbeke et al. 1999, Bartelmann & Schneider 1999b). However, it is also clear that the most challenging issues are observationals, because the measurement of extremely weak gravitational distortions is severely affected by various sources of noise and systematics such as the photon noise, the optical distortion of astronomical telescopes and the atmospheric distortion. Therefore, the problem of reliable shape measurement has also received much attention in the last few years (Bonnet & Mellier 1995, Kaiser et al. 1995, Van Waerbeke et al. 1997, Hoekstra et al. 1998, Kuijken 1999, Rhodes et al. 1999, Kaiser 1999, Bertin 2000).

Despite considerable difficulties in recovering weak lensing signals, the potential cosmological impact of the cosmic shear analysis has motivated several teams to devote efforts on imaging surveys designed for the measurement of the galaxy dis-

Table 1. List of the fields. Most of the exposures were taken in the I band at CFHT. The total area is 1.7 deg^2, and the 8 fields are uncorrelated.

Target	Name	Camera	Used area	Filter	Exp. time	Period	seeing
F14P1	F1	CFH12K	764 arcmin^2	V	5400 sec.	May 1999	0.9″
F14P2	F2	CFH12K	764 arcmin^2	V	5400 sec.	May 1999	0.9″
F14P3	F3	CFH12K	764 arcmin^2	V	5400 sec.	May 1999	0.9″
CFDF-03	F4	UH8K	669 arcmin^2	I	17000 sec.	Dec. 1996	0.75″
SA57	F5	UH8K	669 arcmin^2	I	12000 sec.	May 1998	0.75″
A1942	F6	UH8K	573 arcmin^2	I	10800 sec.	May 1998	0.75″
F02P1	F7	CFH12K	1050 arcmin^2	I	9360 sec.	Nov. 1999	0.8″
F02P4	F8	CFH12K	1050 arcmin^2	I	7200 sec.	Nov. 1999	0.9″

tortion produced by gravitational lensing, either by observing many independent small fields, like the VLT/FORS-I (Maoli et al. in preparation), the HST/STIS (Seitz et al. 1998), the WHT (Bacon et al. 2000), or by observing few intermediate to large fields, like the CFHT/CFH12K-UH8K (this work and Kaiser et al. 2000), the SDSS (Annis et al. 1998) and other on-going surveys. In this paper we present the results of the analysis based on 2 square degrees obtained during previous independent observing runs at the CFHT with mixed I and V colors. This study is part of a our weak lensing survey carried out at CFHT (hereafter the DESCART project[1]) which will cover 16 square degrees in four colors with the CFH12K camera. Though the survey is far from completion, data obtained during previous runs have been used jointly with the first observations of the DESCART survey that we did in May 1999 and in November 1999 in order to demonstrate that the technical issues can be overcome and to better prepare the next observations. This set of data permits us already to report on the detection of a cosmic shear signal.

In the following, we discuss the technique used to extract the cosmological signal and to measure its amplitude and show that systematic effects are well under control. The paper is organized as follows. Sect. 2 describes our data sets. Sect. 3 discusses the details of our PSF correction procedure and Sect. 4 presents the final results. Sect. 5 is devoted to the discussion of the residual systematics and their correction. Sect. 6 presents a preliminary quantitative comparison of our signal with numerical expectations of cosmological scenarios as derived from ray-tracing simulations. Conclusions are given in Sect. 7.

2. Description of the data

The difficulty to get a wide angle coverage of the sky in good conditions is the reason why there is not yet a clear detection of cosmic shear. For this work, we decided to get the widest angular field possible, which was done at the expense of homogeneity of the data set. However this does not impact our primary goals which are the detection of a weak lensing signal and the test of the control of systematics.

We use in total eight different pointings mixing CFH12K and UH8K data sets (see Table 1). They are spread over five statistically independent areas, each separated by more than 10

degrees. The total field covers about 6300 arcmin^2, and contains 3×10^5 galaxies (with a number density $n_g \simeq 30$ gal/arcmin^2). Note that the galaxies are weighted as discussed in Sect. 2.2, and parts of the fields are masked, so the effective number density of galaxies is about half.

All the data were obtained at the CFHT prime focus. We used observations spread over 4 years from 1996 to 1999, with two different cameras: the UH8K (Luppino et al. 1994), covering a field of 28×28 square arc minutes with 0.2 arc-second per pixel and the CFHT12K[2] (Cuillandre et al. 2000) covering a field of 42×28 square arc-minutes with 0.2 arc-second per pixel as well. Because these observations were initially done for various scientific purposes, they have been done either in I or in V band. Table 1 summarizes the dataset. The SA57 field was kindly provided by M. Crézé and A. Robin who observed this field for another scientific purpose (star counts and proper motions). The UH8K Abell 1942 data were obtained during discretionary time. The F14 and F02 fields are part of the deep imaging survey of 16 square-degrees in BVRI being conducted at CFHT jointly by several French teams. This survey is designed to satisfy several scientific programs, including the DESCART weak lensing program, the study of galaxy evolution and clustering evolution, clusters and AGN searches, and prepare the spectroscopic sample to be studied for the VLT-VIRMOS deep redshift survey (Le Fèvre et al. 1998). CFDF-03 is one of the Canada-France-Deep-Fields (CFDF) studied within the framework of the Canada-France Deep Fields, with data collected with the UH8K (Mc Cracken et al. in preparation).

The observations were done as usual, by splitting the total integration time in individual exposures of 10 minutes each, offsetting the telescope by 7 to 12 arc-seconds after each image acquisition. For the I and the V band data, we got between 7 to 13 different exposures per field, all with seeing conditions varying by less than $\pm$ 0.07 arc-seconds (the others were not co-added). The total exposure times range from 1.75 hours in V to 5 hours in I.

The total field observed covers 2.05 square degrees, including 0.88 square degrees in V and 1.17 square degrees in I. However, one CCD of the UH8K and two CCDs initially mounted on the CFH12K of the May 1999 run have strong charge transfer efficiency problems and are not suitable for weak lensing analysis. Therefore, the final area only covers 1.74 square degrees:

---

[1] http://terapix.iap.fr/Descart/

[2] http://www.cfht.hawaii.edu/Instruments/Imaging/CFH12K

0.64 square degrees in V and 1.1 square degrees in I. As we can see from Table 1 each field has different properties (filter, exposure time, seeing) which makes this first data set somewhat heterogeneous.

The data processing was done at the TERAPIX data center located at IAP which has been created in order to process big images obtained with these panoramic CCD cameras[3]. Its CPU (2 COMPAQ XP1000 with 1.2 Gb RAM memory each equipped with DEC alpha ev6/ev67 processors) and disk space (1.2 Tbytes) facilities permit us to handle such a huge amount of data efficiently.

For all but the CFDF-03 field, the preparation of the detrending frames (master bias, master dark, master flats, superflats, fringing pattern, if any) and the generation of pre-reduced and stacked data were done using the FLIPS pre-reduction package (FITS Large Image Pre-reduction software) implemented at CFHT and in the TERAPIX pipeline (Cuillandre et al. in preparation). In total, more than 300 Gbytes of data have been processed for this work.

The CFHT prime focus wide-field corrector introduces a large-scale geometrical distortion in the field (Cuillandre et al. 1996). Re-sampling the data over the angular size of one CCD (14 arc-minutes) cannot be avoided if large angular offsets (> 40 arc-seconds) are used for the dithering pattern (like for the CFDF-03 data). Since we kept the offsets between all individual exposures within a 15 arc-seconds diameter disk, the contribution of the distortion between objects at the top and at the bottom of the CCD between dithered exposures is kept below one tenth of a pixel. With the seeing above 0.7 arc-second and a sampling of 0.2 arc-second/pixel, the contribution of this effect is totally negligible. A simulation of the optical distortion of the instrument shows that the variation from one field to another never exceeds 0.3%, which confirms what we expected from the CFHT optical design of the wide-field corrector. We discuss this point in Sect. 5, in particular by confirming that the sensitivity of the shear components with radial distances is negligible. Also not correcting this optical distortion results in a slightly different plate scale from the center to the edge of the field (pixels see more sky in the outside field). But this is also of no consequence for our program since the effect is very small as compared to the signal we are interested in.

The stacking of the non-CFDF images has been done independently for each individual CCD (each covering 7×14 arc-minutes). We decided not to create a single large UH8K or CFH12K image per pointing since it is useless for our purpose. It complicates the weak lensing analysis, in particular for the PSF correction, and needs to handle properly the gaps between CCDs which potentially could produce discontinuities in the properties of the field. The drawback is that we restricted ourselves to a weak lensing analysis on scales smaller than 7 arc-minutes (radius smaller than 3.5 arc-minutes, as shown in the next figures); this is not a critical scientific issue since the total field of view is still too small to provide significant signal

beyond that angular scale. In the following we consider each individual CCD as one unit of the data set.

The co-addition was performed by computing first the offset of each CCD between each individual exposure from the identification of common bright objects (usually 20 objects) spread over one of the CCD's arbitrary chosen as a reference frame. Then, for each exposure the offsets in the x- and y- directions are computed using the detection algorithm of the SExtractor package (Bertin & Arnouts 1996) which provides a typical accuracy better than one tenth of a pixel for bright objects. The internal accuracy of this technique is given by the rms fluctuations of the offsets of each reference object. Because our offsets were small the procedure works very well and provides a stable solution quickly. We usually reach an accuracy over the CCDs of 0.25 pixels rms (0.05 arc-second) in both directions for offsets of about 10 arc-seconds (50 pixels). Once the offsets are known the individual CCDs are stacked using a bilinear interpolation and by oversampling each pixel by a factor of 5 in both x- and y- directions (corresponding to the rms accuracy of the offsets). The images are then re-binned 1×1 and finally a clipped median procedure is used for the addition. The procedure requires CPU and disk space but works very well, provided the shift between exposures remains small. We then end up with a final set of stacked CCDs which are ready for weak lensing analysis.

The twelve separate pointings of the CFDF-03 field were processed independently using a method which is fully described elsewhere (McCracken et al. 2000, in preparation). Briefly, it uses astrometric sources present in the field to derive a world coordinate system (WCS; in this work we use a gnomic projection with higher order terms). This mapping is then used to combine the eight CCD frames to produce a single image in which a uniform pixel scale is restored across the field. Subsequent pointings are registered to this initial WCS by using a large number of sources distributed over the eight CCDs to correct for telescope flexure and atmospheric refraction. For each pointing the registration accuracy is $\sim 0.05''$ rms over the entire field. The final twelve projected images are combined using a clipped median, which, although sub-optimal in S/N terms, provides the best rejection for cosmic rays and other transient events for small numbers of input images.

3. Galaxy shape analysis

The galaxies have been processed using the IMCAT software generously made available by Nick Kaiser[4]. Some of the process steps have been modified from the original IMCAT version in order to comply with our specific needs. These modifications are described now.

The object detection, centroid, size and magnitude measurements are done using SExtractor (Bertin & Arnouts 1996[5]) which is optimized for the detection of galaxies. We replace the parameter r_g (physical size of an object), calculated in the IMCAT peak finder algorithm by the half-light-radius of SExtractor (which is very similar to r_h measured in IMCAT). This

---

[3] http://terapix.iap.fr/

[4] http://www.ifa.hawaii.edu/~kaiser/
[5] see also ftp://geveor.iap.fr/pub/sextractor/

lowers the signal-to-noise of the shape measurements slightly, but it is not a serious issue for the statistical detection of cosmic shear described in this work. Before going into the details of the shape analysis, we first briefly review how IMCAT measures shapes and corrects the stellar anisotropy. Technical details and proofs can be found in Kaiser et al. 1995 (hereafter KSB), Hoekstra et al. 1998 and Bartelmann & Schneider 1999a.

3.1. PSF correction: the principle

KSB derived how a gravitational shear and an anisotropic PSF affect the shape of a galaxy. Their derivation is a first order effect calculation, which has the nice property to separate the gravitational shear and the atmospheric effects. The correction is calculated first on the second moments of a galaxy, and subsequently the galaxy ellipticity can be directly expressed as a function of the shear and the star anisotropy. The raw ellipticity $\mathbf{e}$ of an object is the quantity measured from the second moments I_{ij} of the surface brightness $f(\boldsymbol{\theta})$:

$$\mathbf{e} = \left(\frac{I_{11} - I_{22}}{Tr(I)}; \frac{2I_{12}}{Tr(I)} \right), \quad I_{ij} = \int \mathrm{d}^2\theta W(\theta)\theta_i\theta_j f(\boldsymbol{\theta}). \quad (1)$$

The aim of the window function $W(\theta)$ is to suppress the photon noise which dominates the objects profile at large radii. According to KSB, in the presence of a shear γ_β and a PSF anisotropy p_β, the raw ellipticity $\mathbf{e}$ is sheared and smeared, and modified by the quantity $\delta\mathbf{e}$:

$$\delta e_\alpha = P^{sh}_{\alpha\beta}\gamma_\beta + P^{sm}_{\alpha\beta}p_\beta. \quad (2)$$

The shear and smear polarization tensors $P^{sh}_{\alpha\beta}$ and $P^{sm}_{\alpha\beta}$ are measured from the data, and the stellar ellipticity $\mathbf{p}$, also measured from the data, is given by the raw stellar ellipticity $\mathbf{e}^\star$:

$$p_\alpha = \frac{e^\star_\alpha}{P^{sm}_{\alpha\alpha}}. \quad (3)$$

Using Eq. (2) and Eq. (3) we can therefore correct for the stellar anisotropy, and obtain an unbiased estimate of the orientation of the shear γ_β. To get the right amplitude of the shear, a piece is still missing: the isotropic correction, caused by the filter $W(\theta)$ and the isotropic part of the PSF, which tend to circularize the objects. Luppino & Kaiser 1997 absorbed this isotropic correction by replacing the shear polarization P^{sh} in Eq(2) (which is an exact derivation in the case of a Gaussian PSF) by the pre-seeing shear polarisability P^γ:

$$P^\gamma = P^{sh} - \frac{P^{sh}_\star}{P^{sm}_\star}P^{sm}. \quad (4)$$

This factor 'rescales' the galaxy ellipticity to its true value without changing its orientation, after the stellar anisotropy term was removed. The residual anisotropy left afterwards is the cosmic shear γ_β, therefore the observed ellipticity can be written as the sum of a 'source' ellipticity, a gravitational shear $\boldsymbol{\gamma}$ term, and a stellar anisotropy contribution:

$$\mathbf{e}^{obs} = \mathbf{e}^{source} + P_\gamma\boldsymbol{\gamma} + P^{sm}\mathbf{p}. \quad (5)$$

There is no reason that $\mathbf{e}^{source}$ should be the *true* source ellipticity $\mathbf{e}^{true}$, as demonstrated by Bartelmann & Schneider 1999a. The only thing we know about $\mathbf{e}^{source}$ is that $\langle \mathbf{e}^{true} \rangle = 0$ implies $\langle \mathbf{e}^{source} \rangle = 0$. Therefore Eq. (5) provides an unbiased estimate of the shear $\boldsymbol{\gamma}$ as long as the intrinsic ellipticities of the galaxies are uncorrelated (which leads to $\langle \mathbf{e}^{true} \rangle = 0$). The estimate of the shear is simply given by

$$\gamma = P_\gamma^{-1} \cdot (\mathbf{e}^{obs} - P^{sm}\mathbf{p}). \quad (6)$$

The quantities P^γ, P^{sm} and $\mathbf{p}$ are calculated for each object. The shear estimate per galaxy (Eq(6)) is done using the matrices of the different polarization tensors, and not their traces (which corresponds to a scalar correction) as often done in the literature. Although the difference between tensor and scalar correction is small (because P_γ is nearly proportional to the identity matrix), we show elsewhere, in a comprehensive simulation paper (Erben et al. 2000), that the tensor correction gives slightly better results.

3.2. PSF correction: the method

The process of galaxy detection and shape correction can be done automatically, provided we first have a sample of stars representative of the PSF. However, in practice the star selection needs careful attention and cannot be automated because of contaminations. Stars can have very close neighbor(s) (for instance a small galaxy exactly aligned with it) that their shape parameters are strongly affected. Therefore we adopted a slow but well-controlled manual star selection process: on each CCD, the stars are first selected in the stellar branch of the $r_g - mag$ diagram in order to be certain to eliminate saturated and very faint stars. We then perform a 3σ clipping on the *corrected* star ellipticities, which removes most of the stars whose shape is affected by neighbors (they behave as outliers compared to the surounding stars). It is worth noting that the σ clipping should be done on the corrected ellipticities and not on the raw ellipticities, since only the corrected ellipticities are supposed to have a vanishing anisotropy. The stellar outliers which survived the σ clipping are checked by eye individually to make sure that no unusual systematics are present.

During this procedure, we also manually mask the regions of the CCD which could potentially produce artificial signal. This includes for example the areas with very strong gradient of the sky background, like around bright stars or bright/extended galaxies, but also spikes produced along the diffraction image of the spider supporting the secondary mirror, columns containing light from saturated stars, CCD columns with bad charge transfer efficiency, residuals from transient events like asteroids which cross the CCD during the exposure and finally all the boundaries of each CCD. At the end, we are left with a raw galaxy catalogue and a star catalogue free of spurious objects, and each CCD chip has been checked individually. This masking process removes about 15% of the CCD area and the selection itself leaves about 30 to 100 usable stars per CCD.

The most difficult step in the PSF correction is Eq. (6), where the inverse of a noisy matrix P^γ is involved. If we do not pay
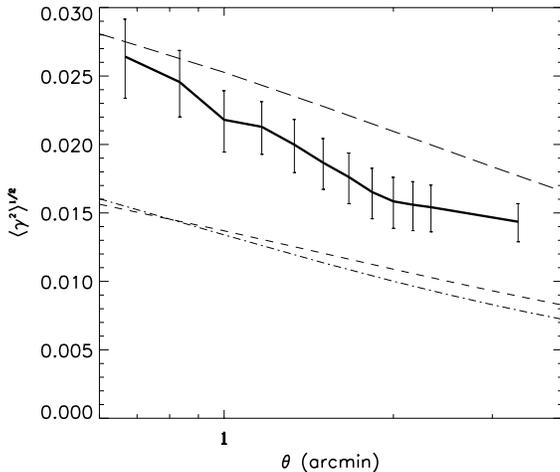
Fig. 1. Square-root of the variance of the measured shear as a function of the radius of the top-hat window (solid line). The maximum angular scale, 3.5 arc-minutes radius, is fixed by the maximum angular scale defined by individual CCDs (7'). Error bars are computed over 1000 random realizations of the galaxy catalogue. The other lines are theoretical predictions of the same quantity for different cosmological models in the non-linear regime (using the fitting formula in Peacock & Dodds 1996): the long-dashed line corresponds to $(\Omega = 1, \Lambda = 0, \sigma_8 = 0.6)$, the dashed line to $(\Omega = 0.3, \Lambda = 0, \sigma_8 = 0.6)$, and the dot-dashed line to $(\Omega = 0.3, \Lambda = 0.7, \sigma_8 = 0.6)$.

attention to this problem, we obtain corrected ellipticities which can be very large and/or negative, which would force us to apply severe cuts on the final catalogue to remove aberrant corrections, thus losing many objects. A natural way to solve the problem is to smooth the matrix P^γ before it is inverted. In principle P^γ should be smoothed in the largest possible parameter space defining the objects: P^γ might depend on the magnitude, the ellipticity, the profile, the size, etc... In practice, it is common to smooth P^γ according to the magnitude and the size (see for instance Kaiser et al. 1998, Hoekstra et al. 1998). Smoothing performed on a regular grid is generally not optimal, and instead, we calculate the smoothed P^γ for each galaxy from its nearest neighbors in the objects parameter space (this has the advantage of finding locally the optimal mesh size for grid smoothing). Increasing the parameter space for smoothing does not lead to significant improvement in the correction (which is confirmed by our simulations in Erben et al. 2000), therefore we keep the magnitude and the size r_h to be the main functional dependencies of P^γ.

A smoothed P^γ does not eliminate all abnormal ellipticities; the next step is to weight the galaxies according to the noise level of the ellipticity correction. Again, this can be done in the gridded magnitude/size parameter space where each cell contains a fixed number of objects (the nearest neighbors method). We then calculate the variance σ_ϵ^2 of the ellipticity of those galaxies, which gives an indication of the dispersion of the ellipticities of the objects in the cell: the larger σ_ϵ^2, the larger the noise. We then calculate a *weight* w for each galaxy, which is directly given by σ_ϵ^2:

$$w = \left\{ \begin{array}{l} \exp(-5(\sigma_\epsilon - \alpha)^2) \text{ if } \sigma_\epsilon < 1 \\ \dfrac{1}{\sigma_\epsilon^2} \exp(-5(1 - \alpha)^2) \text{ if } \sigma_\epsilon > 1 \end{array} \right. , \qquad (7)$$

where α is a free parameter, which is chosen to be the maximum of the ellipticity distribution of the galaxies. Eq. (7) might seem arbitrary compared to the usual $1/\sigma_\epsilon^2$ weighting, but the inverse square weighting tends to diverge for low-noise objects (because such objects have a small σ_ϵ^2), which create a strong unbalance among low noise objects. The aim of the exponential cut-off as defined in Eq. (7) is to suppress this divergence[6].

The weighting function prevents the use of an arbitrary and sharp cut to remove the bad objects. However, we found in our simulations (Erben et al. 2000) that we should remove objects smaller than the seeing size, since they carry very little lensing information, and the PSF convolution is likely to dominate the shear amplitude. Our final catalogue contains about 191000 galaxies, of which 23000 are masked. It is a galaxy number density of about $n \simeq 26 \text{ gal}/\text{arcmin}^2$, although the effective number density when the weighting is considered should be much less. We find $\alpha = 0.5$, which corresponds to the ellipticity variance of the whole catalogue.

4. Measured signal

The quantity directly accessible from the galaxy shapes and related to the cosmological model is the variance of the shear $\langle \gamma^2 \rangle$. An analytical estimate of it using a simplified cosmological model (power-law power spectrum, sources at a single redshift plane, leading order of the perturbation theory, and no cosmological constant) gives (Kaiser 1992, Villumsen 1996, Bernardeau et al. 1997, Jain & Seljak 1997):

$$\langle \gamma^2 \rangle^{1/2} \simeq 0.01 \sigma_8 \Omega_0^{0.75} z_s^{0.75} \left(\frac{\theta}{1 \text{arcmin}} \right)^{-\left(\frac{n+2}{2}\right)}, \qquad (8)$$

where n is the slope of the power spectrum, σ_8 its normalization, z_s the redshift of the sources and θ the top-hat smoothing filter radius. The expected effect is at the percent level, but at small scales the non-linear dynamics is expected to increase the signal by a factor of a few (Jain & Seljak 1997). Nevertheless Eq. (8) has the advantage of clearly giving the cosmological dependence of the variance of the shear.

From the unweighted galaxy ellipticities e_α, an estimate of $\gamma^2(\boldsymbol{\theta}_i)$ at the position $\boldsymbol{\theta}_i$ is given by:

$$E[\gamma^2(\boldsymbol{\theta}_i)] = \sum_{\alpha=1,2} \left(\frac{1}{N} \sum_{k=1}^{N} e_\alpha(\theta_k) \right)^2 . \qquad (9)$$

The inner summation is performed over the N galaxies located inside the smoothing window centered on $\boldsymbol{\theta}_i$, and the outer summation over the ellipticity components. The ensemble average of Eq. (9) is

---

[6] Note that the use of a different weighting scheme like $w \propto 1/(\alpha^2 + \sigma_\epsilon^2)$ has almost no effect on the detection. Other weighting schemes have been used, such as in Hoekstra et al. 2000

$$\langle E[\gamma^2(\boldsymbol{\theta}_i)]\rangle = \frac{\sigma_\epsilon^2}{N} + \langle\gamma^2\rangle. \tag{10}$$

The term σ_ϵ^2/N can be easily removed using a random realization of the galaxy catalogue: each position angle of the galaxies is randomized, and the variance of the shear is calculated again. This randomization allows us to determine σ_ϵ^2/N and the error bars associated with the noise due to the intrinsic ellipticity distribution. At least 1000 random realizations are required in order to have a precise estimate of the error bars. Note that it is strictly equivalent to use an estimator where the diagonal terms are removed in the sum (9), which suppress automatically the σ_ϵ^2/N bias.

When we take into account the weighting scheme for each galaxy, the estimator Eq. (9) has to be modified accordingly as follows:

$$E[\gamma^2(\boldsymbol{\theta}_i)] = \sum_{\alpha=1,2} \left(\frac{\sum_{k=1}^N w(\theta_k)e_\alpha(\theta_k)}{\sum_{k=1}^N w(\theta_k)} \right)^2, \tag{11}$$

where w is the weight as defined in Eq. (7). The variance of the shear is not only the easiest quantity to measure, but it is also fairly weakly sensitive to the systematics provided that they are smaller than the signal. The reason is that any spurious alignment of the galaxies, in addition to the gravitational effect, adds quadratically to the signal and not linearly:

$$\langle\gamma^2_{mes}\rangle = \langle\gamma^2_{true}\rangle + \langle\gamma^2_{bias}\rangle. \tag{12}$$

Therefore, a systematic of say 1% for a signal of 3% only contributes to $\sim 5\%$ in $\langle\gamma^2\rangle^{1/2}$. We investigate in detail in the next sections the term $\langle\gamma^2_{bias}\rangle$ and show that it has a negligible contribution.

We will present results on the shear variance measured from the data sets described in Sect. 2. The variance $\langle\gamma^2_{mes}\rangle$ is measured in apertures which are placed on a 10×20 grid for each of the 2000×4000 CCDs. By construction the apertures never cross the CCD boundaries, and if more than 10% of the included objects turns out to be masked objects, this aperture is not used. Fig. 1 shows $\langle\gamma^2_{mes}\rangle^{1/2}$ (thick line) with error bars obtained from 1000 random realizations. The three other thin lines correspond to theoretical predictions obtained from an exact numerical computation for three different cosmological models, in the non-linear regime. We assumed a normalized broad source redshift distribution given by

$$n(z_s) = \frac{\beta}{z_0\Gamma\left(\frac{1+\alpha}{\beta}\right)} \left(\frac{z_s}{z_0}\right)^\alpha \exp\left(-\left(\frac{z_s}{z_0}\right)^\beta\right), \tag{13}$$

with the parameters $(z_0, \alpha, \beta) = (0.9, 2, 1.5)$ are supposed to match roughly the redshift distribution in our data sets[7]. The shape of this redshift distribution mimics those observed in spectroscopic magnitude-limited samples as well as those inferred from theoretical predictions of galaxy evolution models.

---

[7] with a source redshift distribution which peaks at 0.9

Since we did significant selections in our galaxy catalog the final redshift distribution could be modified. We have not quantified this, but we do not think it would significantly change the average redshift of the sample, even if the shape may be modified. The variance of the shear $\langle\gamma^2\rangle$ is computed via the formula (see Schneider et al. 1998 for the notations):

$$\langle\gamma^2\rangle = 2\pi \int_0^\infty k\mathrm{d}k P_\kappa(k) I_{TH}^2(k\theta), \tag{14}$$

where I_{TH}^2 is the Fourier transform of a Top-Hat window function, and $P_\kappa(k)$ is the convergence power spectrum, which depends on the projected 3-dimensional mass power spectrum $P_{3D}(k)$:

$$P_\kappa(k) = \frac{9}{4}\Omega_0^2 \int_0^{w_H} \frac{\mathrm{d}w}{a^2(w)} P_{3D}\left(\frac{k}{f_K(w)}; w\right) \times$$
$$\int_w^{w_H} \mathrm{d}w' n(w') \frac{f_K(w'-w)}{f_K(w')}. \tag{15}$$

$f_K(w)$ is the comoving angular diameter distance out to a distance w (w_H is the horizon distance), and $n(w(z))$ is the redshift distribution of the sources. The nonlinear mass power spectrum $P_{3D}(k)$ is calculated using a fitting formula (Peacock & Dodds 1996).

We see in Fig. 1 that the measured signal is consistent with the theoretical prediction, both in amplitude and in shape. In order to have a better idea of how significant the signal is we can compare for each smoothing scale the histogram of the shear variance in the randomized samples and the measured signal. This is is shown in Fig. 2, for all the smoothing scales shown in Fig. 1. The signal is significant up to a level of 5.5σ. Note that the measurement points at different scales are correlated, and that an estimate of the overall significance of our signal would require the computation of the noise correlation matrix between the various scales.

5. Analysis of the systematics

Now we have to check that the known systematics cannot be responsible for the signal. In the following we discuss three types of systematics:

- The intrinsic alignment of galaxies which could exists in addition to the lensing effect. We assume such an alignment do not exist, but the overlapping isophotes of close galaxies produces it. We could in principle remove this effect by choosing a window function small compared to the galaxy distance in the pair, such that close galaxies do not influence the second moment calculation of themselves. However this is difficult to achieve in practice.
- The strongest known systematics is the PSF anisotropy caused by telescope tracking errors, the optical distortion, or any imaginable source of anisotropy of the star ellipticity. We have to be sure that the PSF correction outlined in Sect. 2.2 removes any correlation between galaxy and star ellipticities.
- The spurious alignment of galaxies along the CCD frame lines/columns. We cannot reject this possibility since charge
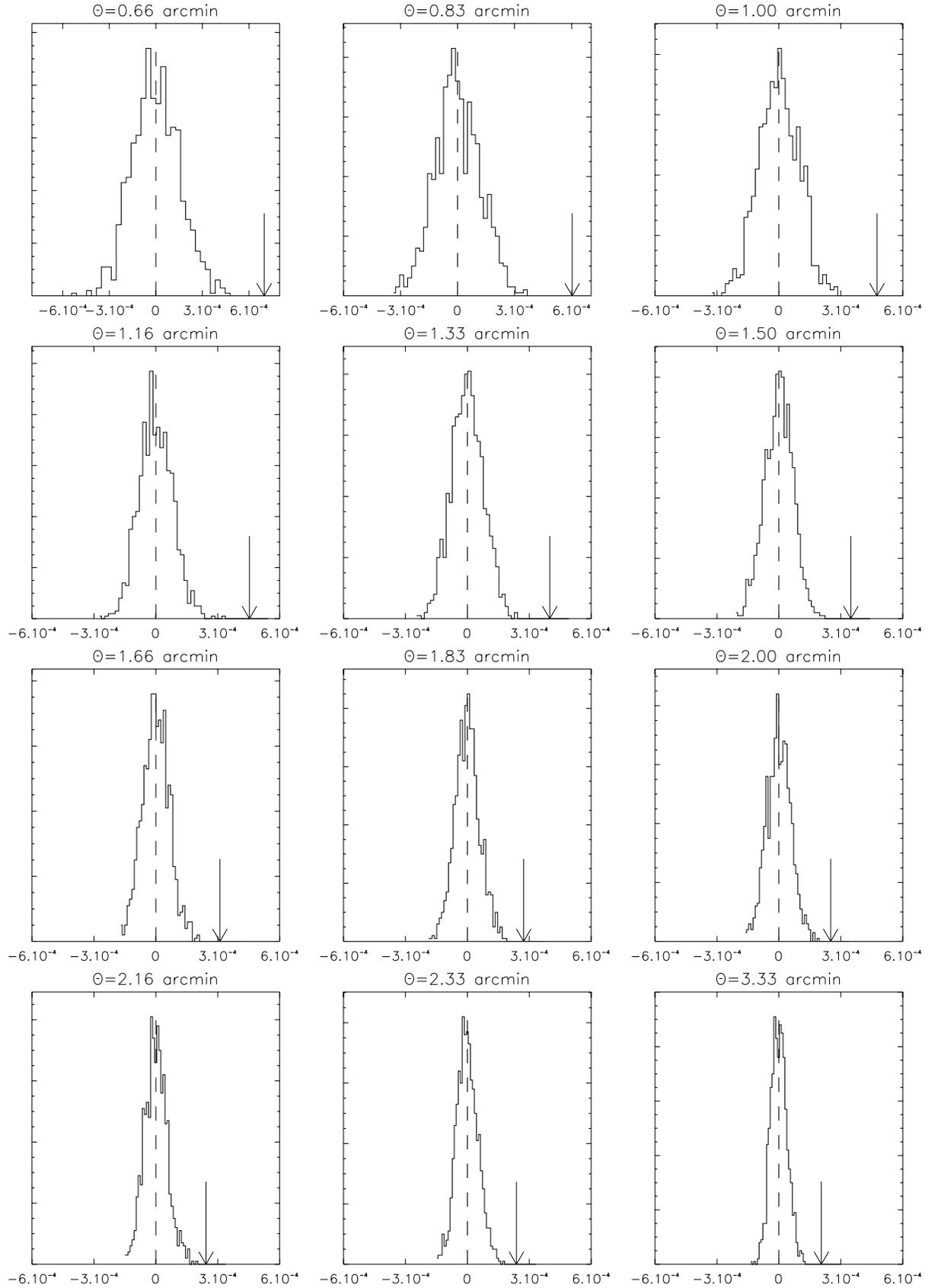
Fig. 2. For different smoothing sizes (indicated at the top of each panel), the value of the measured signal (given by the arrow) compared to the signal measured in the randomized catalogues (histograms). This figure shows how far the signal deviates from a pure random orientation of the galaxies. Note that the distribution of $\langle \gamma^2 \rangle$ is not Gaussian.
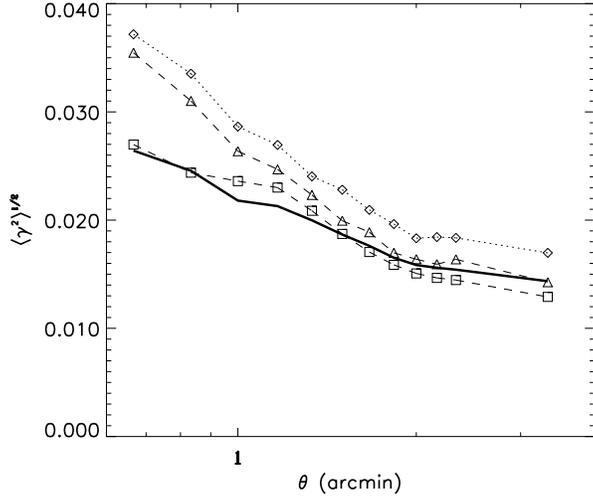
Fig. 3. The thick solid line shows the signal as plotted on Fig. 1. It was obtained with a catalogue of galaxies where galaxies closer than 10 pixels were rejected. The three other curves show the same signal measured with different rejection criteria: the diamond-dotted line is for no rejection at all, the triangle-dashed line for galaxies closer than 5 pixels rejected, and the square-dashed line for galaxies closer than 20 pixels rejected. This figure illustrates that the overlapping isophotes of close galaxies tends to overestimate the shear.

Fig. 4. Average galaxy ellipticity $\langle e_\alpha \rangle$ versus the average star ellipticity $\langle e_\alpha^\star \rangle$ for both components $\alpha = 1, 2$. The dashed lines are obtained from the fully corrected galaxy ellipticities, as given by Eq. (5). The solid lines are obtained from the galaxy ellipticities corrected from the seeing, but without the anisotropy correction term $P^{sm}\mathbf{p}$ of Eq. (5). Each ellipticity bin contains about $N = 16000$ galaxies, and the error bars are calculated assuming Gaussian errors $\propto N$. Except for a constant tiny bias along the e_1 direction, the corrected galaxies are uncorrelated with the stellar ellipticity, which demonstrates that the PSF correction method works well.

transfer along the readout directions is done by moving the charges from one pixel to the next pixel and so forth, with an transfer efficiency of 0.99998. This effect could spread the charges of the bright objects (very bright and saturated stars produce this kind of alignment, but they have been removed during the masking procedure). Therefore we can expect the objects to be elongated along the readout direction.

5.1. Systematics due to overlapping isophotes

Let us consider the first point in the above list of systematics. In order to study the effect of close galaxy pairs, we measured the signal by removing close pairs by varying a cut-off applied on the respective distance of close galaxies. Fig. 3 shows the signal measured when successively closer pairs with $d = 0$ (no pair rejection), 5, 10 and 20 pixels have been rejected. The cases $d = 0$ and $d = 5$ show an excess of power at small scales compared to $d = 10$ and $d = 20$ (the latter two give the same signal). Therefore we assume that for $d > 10$ we have suppressed the overlapping isophote problem, and in the following we keep the $d = 10$ distance cut-off, which gives us a total of ~ 168000 galaxies for the whole data sets, as already indicated at the end of Sect. 3.2. By removing close pairs of galaxies, we also remove the effect of possible alignment of the ellipticities of galaxies in a group due to tidal forces.

5.2. Systematics due to the anisotropic PSF correction

We next study the second point concerning the residual of the PSF correction. Fig. 11 shows that the star ellipticity correction
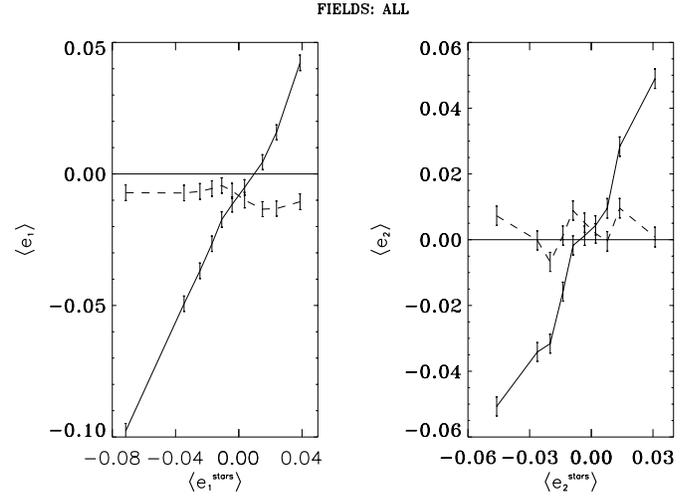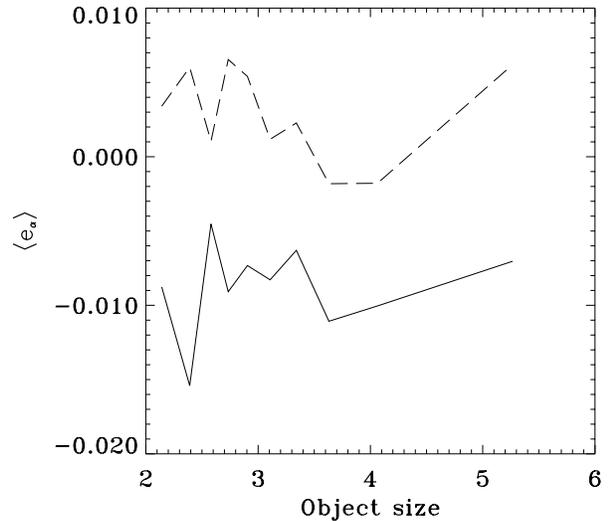

Fig. 5. Average galaxy ellipticity $\langle e_1 \rangle$ (solid line) and $\langle e_2 \rangle$ (dashed line) as a function of the object size r_h. It is shown that the systematic bias of -1% along the e_1 component is fairly galaxy independent.

is efficient in removing PSF anisotropies. The raw star ellipticity can be as large as 20% in the most extreme cases. Figs. 12 to 19 show maps of the uncorrected and the corrected star ellipticities. The same camera used at different times clearly demonstrates that the PSF structure can vary a lot in both amplitude and orientation, and that it is not dominated by the optical distortion (as we can see from the location of the optical center, given by the dashed cross). Individual CCD's are $2K \times 4K$ chips, easily identified by the discontinuities in the stellar ellipticity fields.
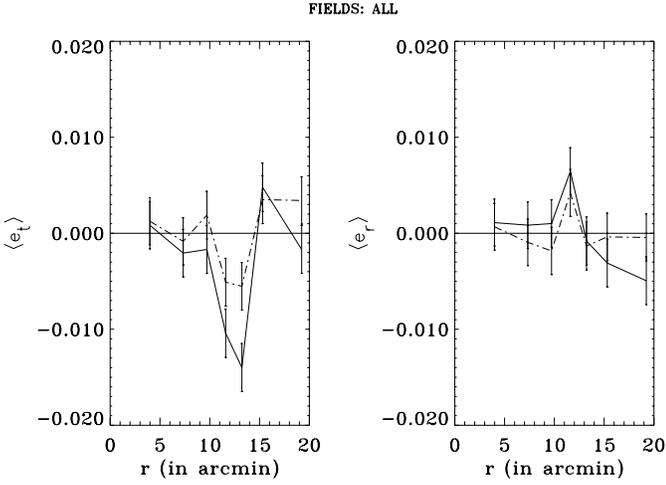
FIELDS: ALL

Fig. 6. Average tangential galaxy ellipticity $\langle \gamma_t \rangle$ and radial galaxy ellipticity $\langle \gamma_r \rangle$ versus the distance from the optical center r. As for Fig. 4, the dashed lines are obtained from the fully corrected galaxy ellipticities, as given by Eq. (5), and the solid lines are obtained from galaxy ellipticities corrected from seeing but where the anisotropy correction term $P^{\mathrm{sm}}\mathbf{p}$ has been removed from Eq. (5). Each ellipticity bin contains about $N = 24000$ galaxies, and the error bars are calculated assuming Gaussian errors $\propto N$. The absence of a significant amplitude between the dashed and the solid lines show that the optical distortion effect is a negligible contribution to the PSF anisotropy.

FIELDS: ALL

Fig. 7. Average galaxy ellipticity $\langle e_\alpha \rangle$ versus the X and Y location on the CCDs. As for Fig. 4, the dashed lines are obtained from the fully corrected galaxy ellipticities, as given by Eq. (5), and the solid lines are obtained from the corrected galaxy ellipticities where the anisotropy correction term $P^{\mathrm{sm}}\mathbf{p}$ has been removed from Eq. (5). The systematic negative mean value of $\langle e_1 \rangle$ along lines or columns of the CCD (the two left panels) show that the galaxies are preferentially aligned with the columns of the CCD in the whole survey. A positive systematic value for $\langle e_2 \rangle$ (the two right panels) is also visible, although much less significant.

Next, let us sort the galaxies according to the increasing stellar ellipticity, and bin this galaxy catalogue such that each bin contains a large number of galaxies. We then measure, for each galaxy bin, two different averaged galaxy ellipticities $\langle e_\alpha \rangle$: one is given by Eq. (5) and the other by Eq. (5), without the anisotropy correction $P^{sm}\mathbf{p}$. The former should be uncorrelated with the star ellipticity if the PSF correction is correct (let us call $\langle e_\alpha \rangle$ this average); and the latter should be strongly correlated with the star ellipticity, (let us call $\langle e_\alpha^{\mathrm{ani}} \rangle$ this average). Since the galaxies are binned according to the stellar ellipticity, galaxies of a given bin are taken from everywhere in the survey, therefore the cosmic shear signal should vanish, and the remaining possible non vanishing value for $\langle e_1 \rangle$ and $\langle e_2 \rangle$ should be attributed to a residual of star anisotropy. Fig. 4 shows $\langle e_1 \rangle$ and $\langle e_2 \rangle$ (dashed lines) and $\langle e_1^{\mathrm{ani}} \rangle$ and $\langle e_2^{\mathrm{ani}} \rangle$ (solid lines) versus respectively $\langle e_1^{\mathrm{stars}} \rangle$ and $\langle e_2^{\mathrm{stars}} \rangle$. The solid lines exhibit a direct correlation between the galaxy and the star ellipticities, showing that the PSF anisotropy does indeed induce a strong spurious anisotropy in the galaxy shapes of a few percents. However, the dashed lines show that the corrected galaxy ellipticities are no longer correlated with the star ellipticity, the average $\langle e_1 \rangle$ fluctuates around -1%, while $\langle e_2 \rangle$ is consistent with zero. This figure shows the remarkable accuracy of the PSF correction method given in KSB. Error bars in these plots are calculated assuming Gaussian errors for the galaxies in a given bin. The significant offset of $\langle e_1 \rangle$ of 1% might be interpreted as a systematic induced by the CCD, as we will see in the next section, and can be easily corrected for. Fig. 5 shows that this systematic is nearly galaxy independent, and affect all galaxies in the same way. This is also
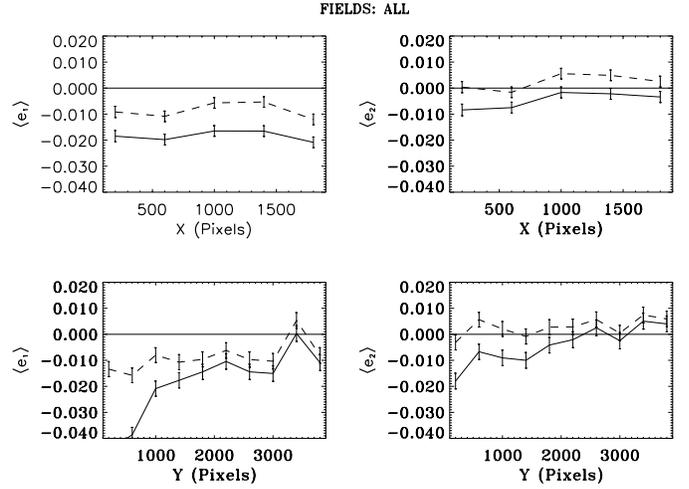
in favor of the CCD-induced systematic, since we expect that a PSF-induced systematic (which is a convolution) would depend on the galaxy size.

Fig. 6 shows the same kind of analysis, but instead of sorting the galaxies according to the star ellipticity amplitude, galaxies are now sorted according to the distance r from the optical center. The average quantities we measure are no longer $\langle e_1 \rangle$ and $\langle e_2 \rangle$ versus $\langle e_1^{\mathrm{stars}} \rangle$ and $\langle e_2^{\mathrm{stars}} \rangle$, but the tangential and the radial ellipticity $\langle e_t \rangle$ and $\langle e_r \rangle$ versus r. This new average is powerful for extracting any systematic associated with the optical distortion. Fig. 6 shows that the systematics caused by the optical distortion are a negligible part of the anisotropy of the PSF, as we should expect from Figs. 12 to 19 (where the PSF anisotropy clearly does not follow the optical distortion pattern).

5.3. Systematics due to the CCD frames

Using the same method as in the previous section, we can also investigate the systematics associated with the CCD line/columns orientations. Here, instead of sorting the galaxies according to the star ellipticity or the distance from the optical center, the galaxies are sorted according to their X or Y location on each CCD frame. By averaging the galaxy ellipticities $\langle e_1 \rangle$ and $\langle e_2 \rangle$ in either X or Y bins, we also suppress the cosmic shear signal and keep only the systematics associated with the CCD frame. Fig. 7 shows $\langle e_1 \rangle$ and $\langle e_2 \rangle$ (dashed lines) and $\langle e_1 \rangle$ and $\langle e_2 \rangle$ (solid lines) versus $\langle X \rangle$ and $\langle Y \rangle$. The plots from the top-left to bottom-right correspond respectively to $\langle e_1 \rangle$ versus $\langle X \rangle$, $\langle e_2 \rangle$ versus $\langle X \rangle$, $\langle e_1 \rangle$ versus $\langle Y \rangle$, and $\langle e_2 \rangle$ versus $\langle Y \rangle$. We see that

$\langle e_1 \rangle$ is systematically negative by $\sim -1\%$ for both X and Y binnings, while $\langle e_2 \rangle$ does not show any significant deviation from zero. This result is fully consistent with the dashed lines in Fig. 4 which demonstrate that the -1% systematic is probably a constant systematic which affects all the galaxies in the same way, and which is not related to the star anisotropy correction. The origin of this constant shift is still not clear, it might have been produced during the readout process, since a negative $\langle e_1 \rangle$ corresponds to an anisotropy along columns of the CCDs.

5.4. Test of the systematics residuals

The correction of the constant shift of -1% along $\langle e_1 \rangle$ has been applied to the galaxy catalogue from the beginning. It ensures that there is no more significant residual systematic (either star anisotropy or optical distortion or CCD frame), and demonstrates that the average level of residual systematics is small and much below the signal. However we have to check that the systematics do not oscillate strongly around this small value. If it were the case, then this small level of systematics could still contribute significantly to the variance of the shear. This can be tested by calculating the variance of the shear in bins much smaller than those used in Fig. 4 to calculate the average level of residual systematics. In order to decide how small the bins should be we can use the number of galaxies available in the apertures used to measure the signal, for a given smoothing scale. For example for $\theta = 0.66'$ there is 45 galaxies in average, and for $\theta = 3.3'$ there is 1100 galaxies. We can therefore translate a bin size into a smoothing scale, via the mean number of galaxies in the aperture. We found that the variance of the shear measured in these smaller bins is still negligible with respect to the signal, as shown by Fig. 8. The three panels from top to bottom show respectively the star anisotropy case, the optical distortion case and the CCD frame case. On each panel, the thick solid line is the signal with its error bars derived from 1000 randomizations. The short dashed lines show the $\pm 1\sigma$ of these error bars centered on zero. On the top panel the two thin solid lines show $\langle \gamma^2 \rangle$ respectively measured with the galaxies sorted according to e_1^{stars} and to e_2^{stars}. The thin solid line in the middle panel shows $\langle \gamma_t^2 \rangle$ measured from the galaxies, sorted according to their distance from the optical center, and the two thin solid lines in the bottom panel show $\langle \gamma^2 \rangle$ measured on the galaxies sorted according to X and Y.

In all the cases, the thin solid lines are consistent with the $\pm 1\sigma$ fluctuation, without showing a significant tendency for a positive $\langle \gamma^2 \rangle$. We conclude that the residual systematics are unable to explain the measured $\langle \gamma^2 \rangle$ in our survey, and therefore our signal is likely to be of cosmological origin.

A direct test of its cosmological origin is to measure the correlation functions $\langle e_t(0)e_t(\theta) \rangle$, $\langle e_r(0)e_r(\theta) \rangle$ and $\langle e_r(0)e_t(\theta) \rangle$, where e_t and e_r are the tangential and radial component of the shear respectively:

$$e_t = -e_1 \cos(2\theta_k) - e_2 \sin(2\theta_k)$$
$$e_r = -e_2 \cos(2\theta_k) + e_1 \sin(2\theta_k), \tag{16}$$

Table 2. List of the ray tracing simulations we used (see Jain et al. 1999 for details). The redshift of the sources is 1.

Simulation #	Γ	Ω_0	Λ	σ_8
(1) OCDM	0.21	0.3	0	0.85
(2) τCDM	0.21	1	0	0.6
(3) τCDM	0.21	1	0	1

where θ_k is the position angle of a galaxy. If the signal is due to gravitational shear, we can show (Kaiser 1992) that $\langle e_t(0)e_t(\theta) \rangle$ should be positive, $\langle e_r(0)e_r(\theta) \rangle$ should show a sign inversion at intermediate scales, and $\langle e_r(0)e_t(\theta) \rangle$ should be zero. This is a consequence of the scalar origin of the gravitational lensing effect and of the fact that galaxy ellipticity components are uncorrelated. Although we do not yet have enough data to perform an accurate measurement of these correlation functions, it is interesting to check their general behavior. Fig. 9 shows that in our data set, although the measurement is very noisy, both $\langle e_t(0)e_t(\theta) \rangle$ and $\langle e_r(0)e_r(\theta) \rangle$ are positive valued, while $\langle e_r(0)e_t(\theta) \rangle$ is consistent with zero. This measurement demonstrates that the component of the galaxy ellipticities e_α of well separated galaxies are uncorrelated, and it is in some sense a strong indication that our signal at small scales is of cosmological origin.

The last thing we have checked is the stability of the results with respect to the field selection. We verified that removing one of the fields consecutively for all the fields (see Sect. 2 for the list of the fields) does not change the amplitude and the shape of the signal, even for the Abell 1942 field. The cluster has no impact and does not bias the analysis because it was significantly offset from the optical axis. This ensures that the signal is not produced by one field only, and that they are all equivalents in terms of image quality, PSF correction accuracy and signal amplitude, even using V and I colors. It also validates the different pre-reduction methods used for the different fields.

6. Cosmological constraints

Fig. 1 provides a first comparison of our signal with some cosmological models. In order to rule out models we need to estimate first the sample variance in the variance of the shear. Although it has not been yet exactly derived analytically (because calculations in the non-linear regime are difficult), ray-tracing simulations can give an accurate estimate of it. We used the ray-tracing simulations of Jain et al. 1999 for this purpose.

Table 2 shows the two simulations we used. The τCDM model with $\sigma_8 = 1$ is not an independent simulation, but was constructed from the τCDM model with $\sigma_8 = 0.6$ simply by dividing κ by 0.6. This should empirically mimic a model with both Ω_0 and σ_8 equal to one. The redshift of the sources is equal to 1, which is not appropriate for our data. However, for the depth of the survey, we believe that it represents fairly well the mean redshift of the galaxies, which is the dominant factor in determining the second moment. Fig. 10 shows the amplitude and the scale dependence of the variance of the shear for the three
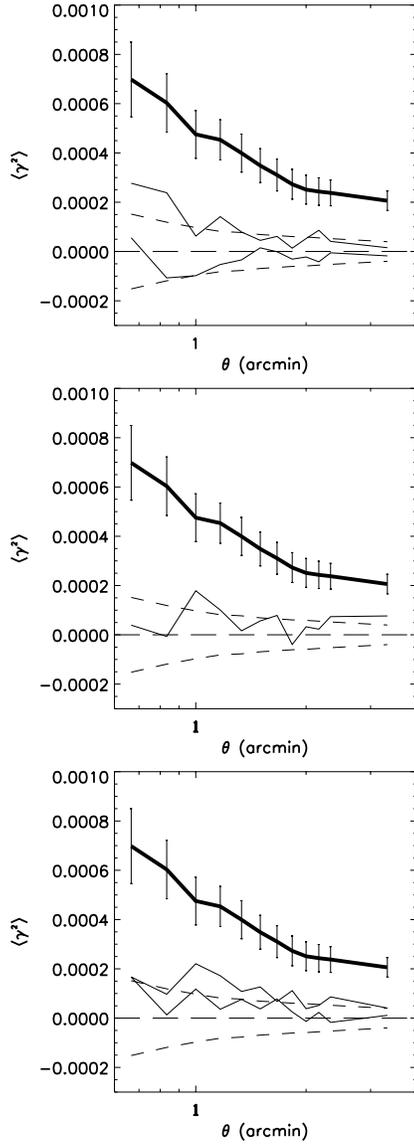
Fig. 8a–c. Possible contribution of the systematics studied in Sect. 3.2 to the signal. On each of the plots, the thick solid line shows the signal as displayed in Fig. 1, and the dashed lines show the $\pm 1\sigma$ fluctuation obtained from 1000 random realizations. From top to bottom: **a** The two thin solid lines are $\langle \gamma^2 \rangle^{1/2}$ measured on the galaxies sorted according to the star ellipticity strength (see Fig. 4). For the different smoothing scales, the mean number and the variance of the number of galaxies in the chosen bins fit the one observed in the signal (thick solid) curve. **b** the thin solid line is $\langle \gamma_t^2 \rangle^{1/2}$ measured on the galaxies sorted according to the distance from the optical center, and on **c** the two thin solid lines correspond to the galaxies sorted according to their X or Y location on the CCDs.

cosmological models, compared to our signal. It is remarkable that models (1) and (3) can be marginally rejected (We did not plot the error bars due to the intrinsic ellipticity for clarity: they can be obtained from Fig. 8).

Our measurements are in agreement with the cluster normalized model (2). Also plotted is the theoretical prediction of a ΛCDM model, with $\Omega = 0.3$, $\Lambda = 0.7$, $\Gamma = 0.5$ and
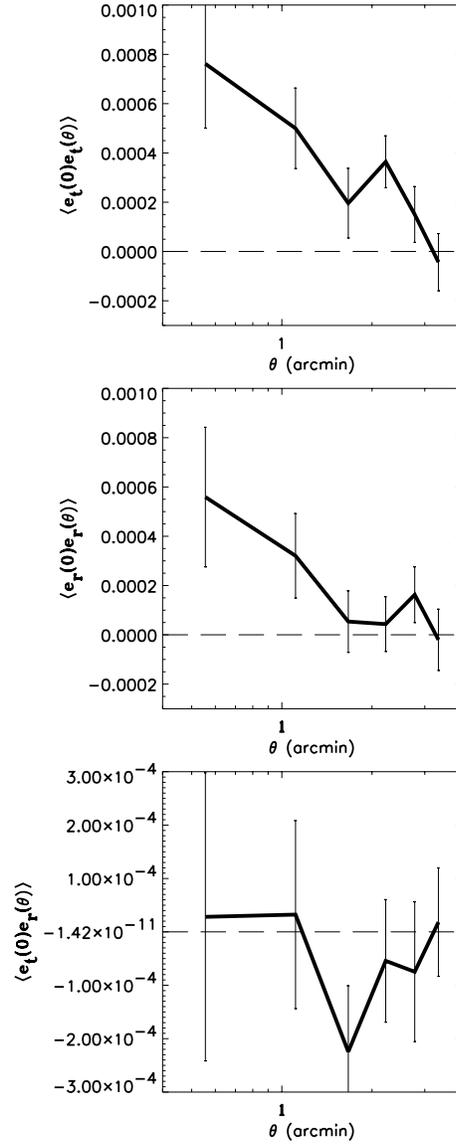
Fig. 9. From top to bottom, measurement of the correlation functions $\langle e_t(0)e_t(\theta) \rangle$, $\langle e_r(0)e_r(\theta) \rangle$ and $\langle e_r(0)e_t(\theta) \rangle$. The error bars are computed from 50 random realizations of our data set where the orientations of the galaxies were randomized.

a redshift of the sources $z_s = 1$. It shows that the low-Ω model is also in good agreement with the data, which means that weak gravitational lensing provides cosmological constraints similar to the cluster abundance results (Eke et al. 1996, Blanchard et al. 1999): the second moment of the shear measures a combination of σ_8 and Ω_0 (see Eq. 8). A measure of the third moment of the convergence would break the Ω-σ_8 degeneracy, but this requires more data (see Bernardeau et al. 1997, Van Waerbeke et al. 1999, Jain et al. 1999). It should also be noted that for the simulations, we have considered cold dark matter models with shape parameter $\Gamma = 0.21$; higher values of Γ increase the theoretical predictions on scales of interest, e.g. the $\Omega_0 = 1$, $\sigma_8 = 1$ model would be ruled out even more strongly. We conclude that our analysis is consistent with the
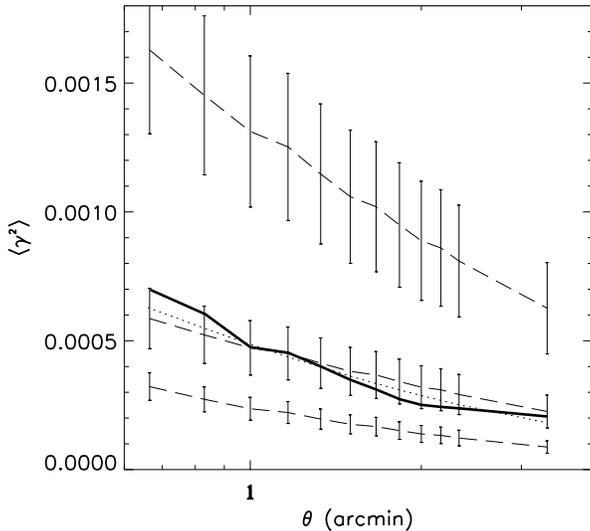
Fig. 10. Comparison of our signal (thick line) with three cosmological models. The error bars are the cosmic variance measured on five independent realizations at the smoothing scale indicated by the x-axis. For clarity, the shot noise error bars of the signal are not plotted, their amplitude can be read in Fig. 8. From bottom to top, the dashed lines correspond to: model (1), model (2) and model (3) as given in Table 2. The shot-noise error bars of the signal are in fact comparable in amplitude to the cosmic variance error bars of model (2). We show also a cluster-normalized Λ model (dotted line) with $\Omega = 0.3$, $\Lambda = 0.7$, and a CDM power spectrum with $\Gamma = 0.5$. This model was not obtained from a simulation, but computed using the non-linear power spectrum using the Peacock & Dodds 1996 formula.

current favored cosmological models, although we cannot yet reject other models with high significance. Since we have only analyzed 2 square degrees of the survey, with forthcoming larger surveys we should be able to set strong constraints on the cosmological models as discussed below.

Due to the imprecise knowledge of the redshift distribution in our data, the interpretation might still be subject to modifications. The final state of our survey in 4 colors will however permit the measurement of this distribution by estimating photometric redshifts for the source galaxies.

7. Conclusion

We have demonstrated the existence of a significant correlation between galaxy ellipticities from 0.5 to 3.5 arc-minutes scales. The signal has the amplitude and the angular dependence expected from theoretical predictions of weak lensing produced by large-scale structures in the universe. We have tested the possible contribution of systematic errors to the measured signal; in particular we discussed three potential sources of spurious alignment of galaxies: overlapping isophotes of very close galaxies, star anisotropy and CCD line/column alignment. The first of these systematics is easy to deal with, simply by removing close pairs, although we may have decreased the signal slightly by removing them. The star anisotropy seems to be very well controlled, in part due to the fact that the bias adds quadrat-
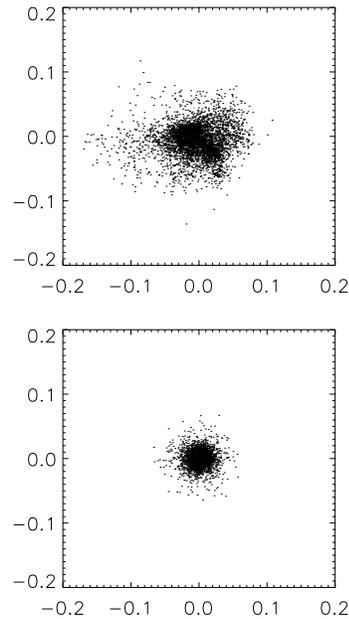

Fig. 11. Star ellipticities of all the survey before (top panel) and after (bottom panel) the correction. After correction, the star ellipticity is randomly distributed around zero, as expected.

ically with the signal. Moreover, in the absolute sense, the bias does not exceed a fraction of 1 percent, which is adequate to accurately measure a variance of the shear of few percent. The only important bias we found seems to be associated with the CCD columns, and it is constant over the survey, it is therefore easy to correct for. The origin of this CCD bias is still unclear.

As an objective test of the reality of the gravitational shear signal, we measured the ellipticity correlation functions $\langle e_t(0)e_t(\theta)\rangle$, $\langle e_r(0)e_r(\theta)\rangle$ and $\langle e_r(0)e_t(\theta)\rangle$. While the measurement is noisy, the general behavior is fully consistent with the lensing origin of the signal. The tests for systematic errors and the three ellipticity correlation function measurements described above have led us to conclude with confidence that we have measured a cosmic shear signal.

With larger survey area, we expect to be able to measure other lensing statistics, like the aperture mass statistic (M_{ap}; see Schneider et al. 1998). The M_{ap} statistic is still very noisy for our survey size because its signal-to-noise is lower than the top-hat smoothing statistic, due to higher sample variance (We verified this statement using the ray tracing simulation data of Jain et al. 1999). Our survey will increase in size in the near future (quickly up to 7 square degrees), leading to a factor of 2 improvement in the signal-to-noise of the results presented here. According to our estimates, this will be enough to measure M_{ap} at the arc-minute scale with a signal-to-noise of ~ 3. The detection of the skewness of the convergence should also be possible with the increased survey area. This will be important in breaking the degeneracy between the amplitude of the power spectrum and Ω (Bernardeau et al. 1997, Van Waerbeke et al. 1999, Jain et al. 1999). These measures should also provide nearly independent confirmations of the weak gravitational lensing effect as well as additional constraints on cosmology. Thus by com-
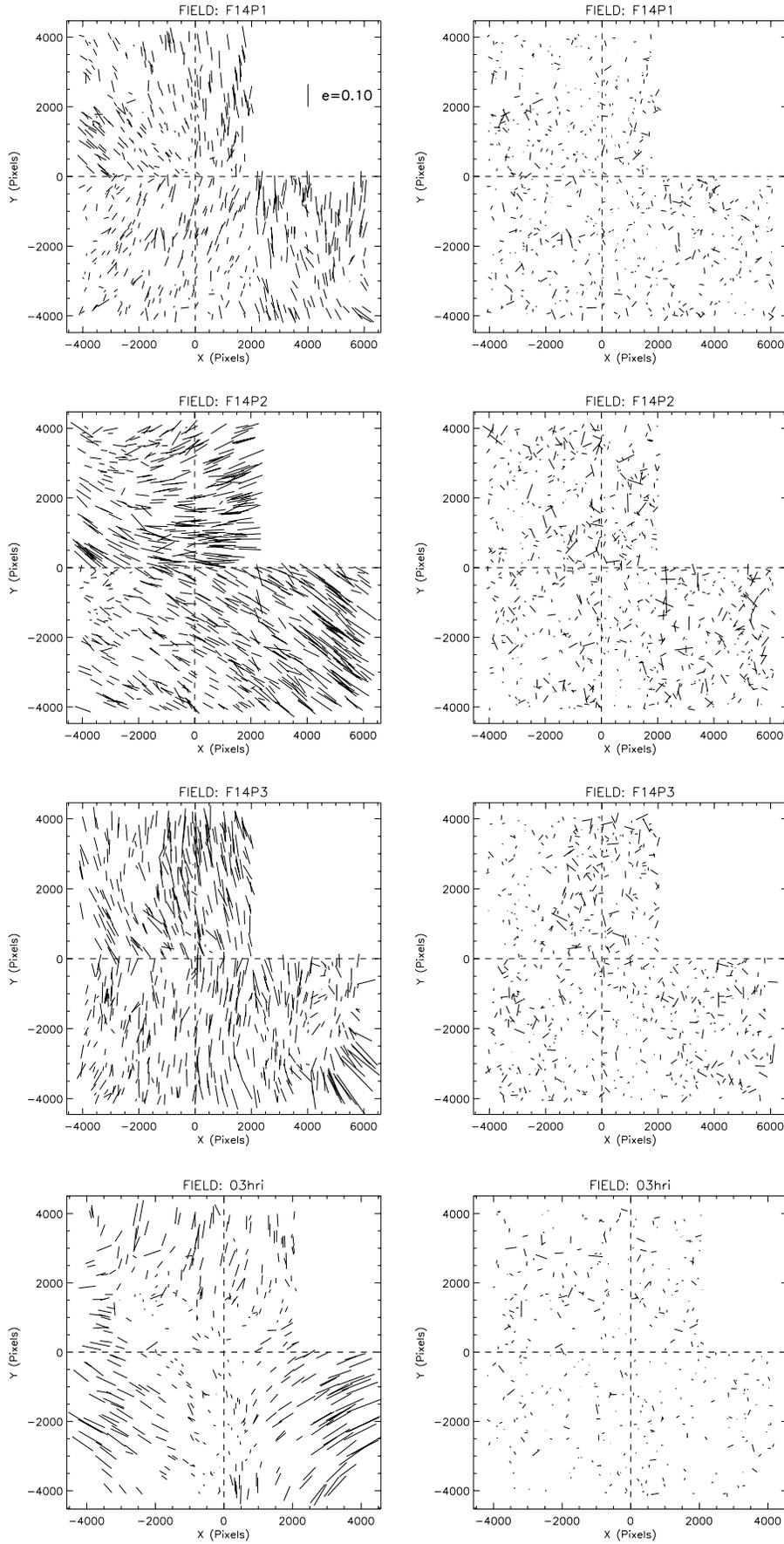
Fig. 12. Uncorrected (left) and corrected (right) star ellipticities for FIELD F14P1. The dashed cross shows the location of the optical center. Frames are graduated in pixels. The reference stick at the top-left of the frame shows the amplitude of a 10% distortion. This length of reference applies also for Figs. 13 to 19.

Fig. 13. Same as Fig. 12 for FIELD F14P2.

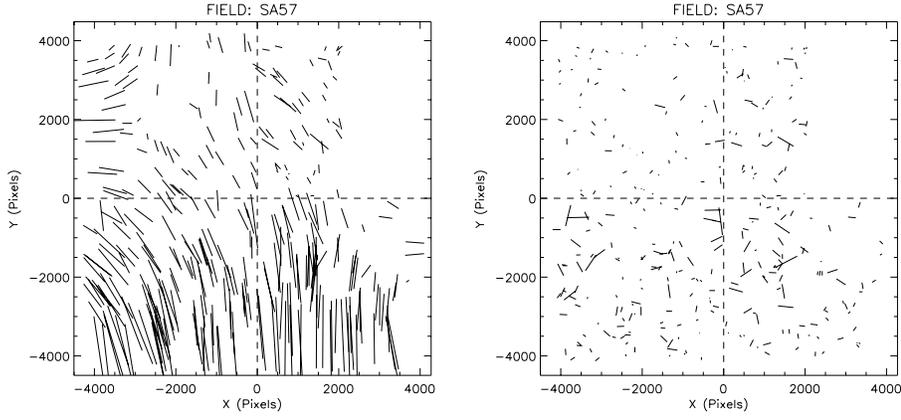**Fig. 14.** Same as Fig. 12 for FIELD F14P3.

Fig. 15. Same as Fig. 12 for FIELD 03hrie.

Fig. 16. Same as Fig. 12 for FIELD SA57.
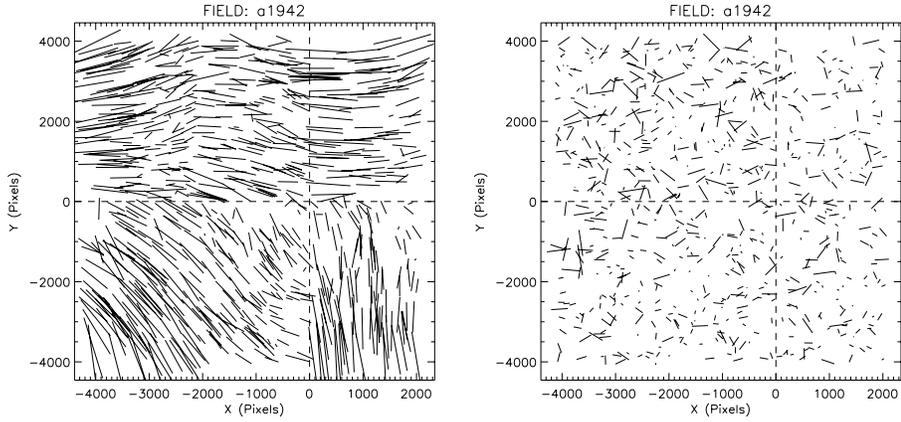
Fig. 17. Same as Fig. 12 for FIELD a1942.
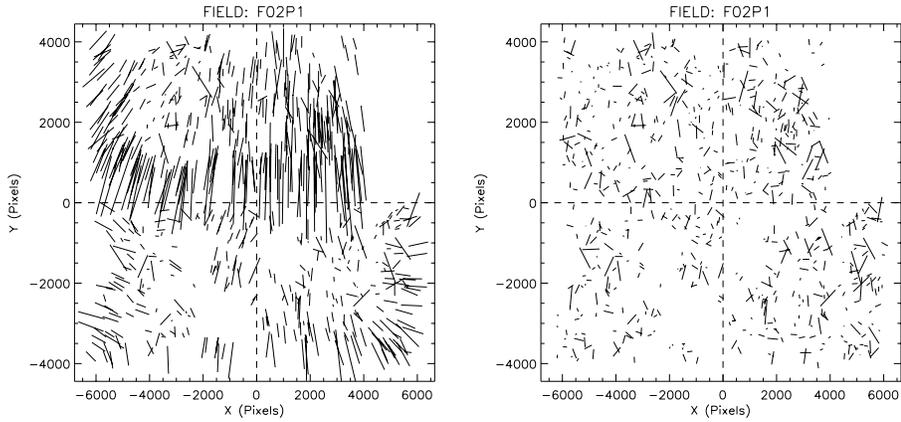
Fig. 18. Same as Fig. 12 for FIELD F02P1.
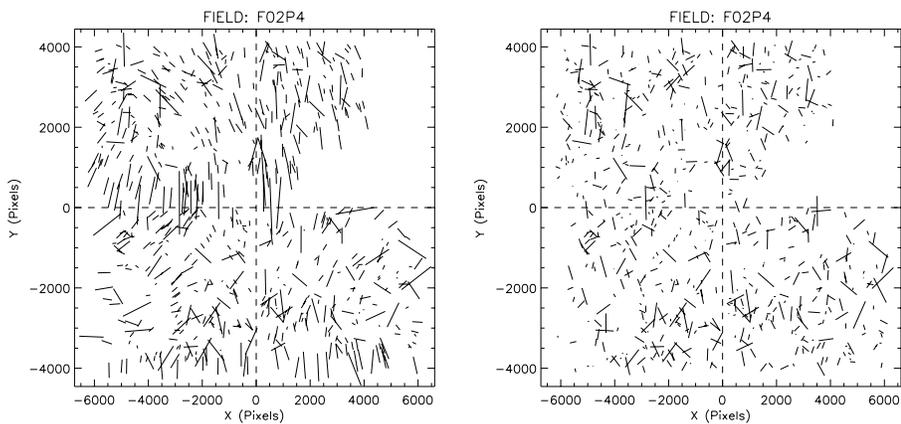
Fig. 19. Same as Fig. 12 for FIELD F02P4.

bining different measures of lensing by large-scale structure (top-hat smoothing statistics, M_{ap} statistics, correlation function analysis, power spectrum measurements), higher order moments, and peak statistics (Jain & Van Waerbeke 2000), from forthcoming survey data, we hope to make significant progress in measuring dark matter clustering and cosmological parameters with weak lensing.

We also hope to do a detailed analysis with a more sophisticated PSF correction algorithm. For instance, the mass reconstruction is linear with the amplitude of the residual bias, and a fraction of percent bias is still enough to prevent a definitive detection of filaments or to map the details of large scale structures. Since we show elsewhere (Erben et al. 2000) that such a bias is unavoidable with the present day correction techniques and image quality, there is still room to improve the analysis prior to obtaining accurate large-scale mass maps. Recent efforts to improve the PSF correction are very encouraging (Kaiser 1999). We plan to explore such approaches once we get an essentially homogeneous data set on a larger field.

References

Annis J., Frieman J., Joffre M., et al., 1998, In: Colombi S., Mellier Y., Raban B. (eds.) Wide Field Surveys in Cosmology. Frontières

Bartelmann M., Schneider P., 1999b, A&A 345, 17

Bartelmann M., Schneider P., 1999a, astro-ph/9912508

Bacon D., Refregier A., Ellis R., 2000, astro-ph/0003008

Bertin E., 2000, in preparation

Bertin E., Arnouts S., 1996, A&A 117, 393

Bernardeau F., Van Waerbeke L., Mellier Y., 1997, A&A 322, 1

Blanchard A., Sadat R., Bartlett J., Le Dour M., 1999, astro-ph/9908037

Blandford R., Saust A., Brainerd T., Villumsen J., 1991, MNRAS 251, 600

Bonnet H., Mellier Y., 1995, A&A 303, 331

Cuillandre J.-C., Mellier Y., Dupin J.-P., et al., 1996, PASP 108, 1120

Cuillandre J.-C., Luppino G., Starr B., Isani S., 2000, In: Amico P., Beletic J.W. (eds.) Optical Detectors for Astronomy. ASSL Series. Kluwer 2000

Eke V.R., Cole S., Frenk C.S., 1996, MNRAS 282, 263

Erben T., et al. in preparation

Hoekstra H., Franx M., Kuijken K., 2000, astro-ph/9910487

Hoekstra H., Franx M., Kuijken K., Squires G., 1998, ApJ 504, 636

Jain B., Seljak U., 1997, ApJ 484, 560

Jain B., Seljak U., White S., 1999, ApJ 530, 547

Jain B., Van Waerbeke L., 2000, ApJ 530, L1

Kaiser N., 1992, ApJ 388, 272

Kaiser N., 1998, ApJ 498, 26

Kaiser N., 1999, ApJ submitted, astro-ph/9904003

Kaiser N., Squires G., Broadhurst T., 1995, ApJ 449, 460

Kaiser N., Wilson G., Luppino G., 2000, astro-ph/0003338

Kaiser N., Wilson G., Luppino G., et al., 1998, ApJ submitted, astro-ph/9809268

Kuijken K., 1999, A&A 352, 355

Le Fèvre O., Vettolani G., Maccagni D., et al., 1998, In: Colombi S., Mellier Y., Raban B. (eds.) Wide Field Surveys in Cosmology. Frontières

Luppino G., Bredthauer R., Geary J. C., 1994, SPIE 2198, 810

Luppino G., Kaiser N., 1997, ApJ 475, 20

Mellier Y., 1999, ARA&A 37, 127

Miralda-Escude J., 1991, ApJ 380, 1

Peacock J.A., Dodds S.J., 1996, MNRAS 280, L9

Rhodes J., Refregier A., Groth E., 1999, ApJ submitted, astro-ph/9905090

Schneider P., Van Waerbeke L., Jain B., Kruse G., 1998, MNRAS 296, 873

Seitz S., Collodel L., Pirzkal N., et al., 1998, In: Colombi S., Mellier Y., Raban B. (eds.) Wide Field Surveys in Cosmology. Frontières

Van Waerbeke L., Mellier Y., Schneider P., Fort B., Mathez G., 1997, A&A 317, 303

Van Waerbeke L., Bernardeau F., Mellier Y., 1999, A&A 342, 15

Villumsen J., 1996, MNRAS 281, 369